IEEE Access
Multidisciplinary ⋮ Rapid Review ⋮ Open Access Journal

Received October 23, 2018, accepted November 11, 2018, date of publication November 27, 2018,
date of current version January 7, 2019.

Digital Object Identifier 10.1109/ACCESS.2018.2883297

Cone-Beam Computed Tomography Deblurring Using an Overrelaxed Chambolle-Pock Algorithm

CHEN LUO[1], QIAO LIU[1], SHUTAO GONG[1,2], CHUNLIN YANG[1], XIUHUA HU[3], KE NIE[4], AND TIANYE NIU[1,2]

[1]Sir Run Run Shaw Hospital, Zhejiang University School of Medicine, Institute of Translational Medicine, Zhejiang University, Hangzhou 310016, China
[2]Key Laboratory of Biomedical Engineering, Ministry of Education, College of Biomedical Engineering and Instrument Science, Zhejiang University, Hangzhou 310009, China
[3]Department of Radiology, Sir Run Run Shaw Hospital, Zhejiang University School of Medicine, Hangzhou 310016, China
[4]Department of Radiation Oncology, Rutgers—Cancer Institute of New Jersey, Rutgers—Robert Wood Johnson Medical School, New Brunswick, NJ 08903, USA

Corresponding authors: Ke Nie (kn231@cinj.rutgers.edu) and Tianye Niu (tyniu@zju.edu.cn)

This work was supported in part by the National High-tech R&D Program for Young Scientists by the Ministry of Science and Technology of China under Grant 2015AA020917, in part by the National Key Research Plan by the Ministry of Science and Technology of China under Grant 2016YFC0104507, in part by the Natural Science Foundation of China (NSFC) under Grant 81871351, Grant 81201091, and Grant 51305257, in part by the Zhejiang Provincial Natural Science Foundation of China under Grant LR16F010001 and Grant LY16H180001, in part by the Fund Project for Excellent Abroad Scholar Personnel in Science and Technology, in part by the Zhejiang University Education Foundation ZJU-Stanford Collaboration Fund, and in part by the Medical Health Science and Technology Project of the Zhejiang Provincial Health Commission under Grant 2019RC189.

ABSTRACT The scatter contamination and photon starvation artifacts are less severe due to the smaller cone angle and attenuation associated with the smaller sample size in the microstructure imaging (MSI) with a cone-beam CT (CBCT) instrument. Compared with other artifacts, the blurring effect is more critical in the MSI due to the direct degradation of spatial resolution. An efficient deblurring method using the line integral images is proposed in this paper. The point spread function (PSF) of the CBCT system is simplified as a 2D Gaussian kernel function with the spatially invariant assumption. The deblurred line integral images are calculated using the iterative optimization process with an objective function in which the blurring effects are described by the convolution between the simplified PSF and the real line integral image. A first-order primal–dual algorithm is applied and derived to solve the real line integral image due to its fast convergence and high computational efficiency. The performance of the proposed method is evaluated using various datasets, including a digital phantom, a physical phantom, and a laboratory mouse. The spatial resolution, noise distribution, and computation cost of the proposed method are compared with those of a 3D image domain deconvolution method. In addition to the well-suppressed blurring effects in the CBCT images, the proposed method provides a higher computational efficiency than the 3D approach. The proposed method is thus practical and attractive to be incorporated into the data processing workflow of the CBCT instrument of MSI.

INDEX TERMS Computed tomography, deconvolution, spatial resolution.

I. INTRODUCTION

The major advantages of the cone-beam computed tomography (CBCT) over the multi-slice computed tomography (MSCT) include the high isotropic spatial resolution, the flexibilities in the geometry configuration and the volumetric coverage in one rotation [1]. Recently, the application of CBCT in the preclinical research including the small animal imaging [2] and the ex-vivo bone analysis [3] is enabled by these advantages which are essential in the microstructure imaging (MSI). In general, there are various physical factors which strongly degrade the image quality of the CBCT instrument and lead to images artifacts, including scatter contamination [4]–[8], beam hardening [9]–[13], photon starvation [14] and blurring effect [15], [16]. Due to the much smaller size of the object in the preclinical application compared with that in the human scan in the clinical environment, the scatter contamination and photon starvation artifacts in the preclinical application are less severe due to the smaller cone angle and illuminated volume. The beam hardening artifact is reduced by the x-ray spectrum-dependent selection

of the metal filtrations embedded into the source of the CBCT equipment [17]. To resolve the microstructures using the CBCT scanner in the preclinical application, it is essential to suppress the blurring effect which leads to the direct degradation of the system spatial resolution. The major factors of the blurring effects in the CBCT equipment [15], [16] include the finite x-ray focal spot size and detector element aperture, and the photon spreading effect in the scintillator. The suppression of the blurring effects, namely the deblurring process, is designed to suppress the effect caused by multiple factors.

There are two major approaches in the current deblurring solutions, including the hardware upgrades of the existing CBCT equipment and the image processing algorithms based on the modeling of the physics process of the blurring effects. The spatial resolution of a CBCT imaging system can be directly improved by the upgrade of the system components using the x-ray tube of smaller focal spot and the flat panel detector of smaller pixel size [15]. The most common option of the x-ray source upgrade is using the micro-focus x-ray tube with smaller focal spot size. Since the current and power of the micro-focus tube are much less than the regular tube, the prolonged integration time of the exposure is required to achieve a reasonable signal-to-noise ratio (SNR), leading to motion artifacts in the in-vivo scans where the anesthesia duration is limited. Decreasing the size of each pixel on the detector is another option to increase the spatial resolution. Nevertheless, two issues are associated with the smaller pixel size, including the increased computation load for the same field of view (FOV) and the lower SNR due to the decreased sensitive area of the detector unit. The limitations and difficulties in the above hardware upgrading methods stimulate the research of advanced image processing algorithms where the higher spatial resolutions were achieved using the mathematical deblurring models in the existing CBCT instruments [16], [18]–[20]. In the development of the deblurring algorithms for a CBCT instrument, the point spread function (PSF) is widely used to quantitatively characterize the performance of the CBCT system. The PSF, representing the impulse response of a complete imaging system, is a mathematical term that describes the blurring effect in the imaging system [15]. In the two-dimensional (2D) case such as the projection domain image, the measured image is the convolution between the real image and the PSF of the CBCT system [21]. The current methods of the CT image deblurring are divided into two categories including the projection and the image domain methods.

The projection domain deblurring methods build the model of the blurring effects from the physical factors in the x-ray projection, including the finite focal spot, the detector aperture, and the photon spreading effect [22]. Tilley *et al.* [16] developed a forward model for the CBCT imaging system where a flat panel detector was used. The blurring effects due to the finite focal spot size and the indirect measurement of x-ray through the detector scintillator were described by the blurring matrix in the forward model. The deblurring process for the projections is composed of the inversion of the blurring matrix. The deblurred projections were reconstructed by a penalized generalized least-squares algorithm [16]. The blurring effects in the reconstructed CBCT images were well suppressed using Tilley's method. When the detector blur was comparable to the source blur, limited deblurring performance was observed using Tilley's method since it fails to include the blurring effect due to the finite detector aperture. In general, the precisely modeled blurring effect of the system is a necessary prerequisite to the efficient deblurring operation in the projection domain deblurring. The characterization of each blurring effect in the mathematical model is complicated due to the complexity in the physical factors underneath the blurring effects and the flexibility in the system configuration.

Compared with the projection methods, the modeling in the image domain deblurring methods is more straightforward. The real image is estimated using the inversed convolution, namely the deconvolution between the measured image and the impulse response of the CBCT imaging system characterized by a systematic PSF. To combat for the blurring issue in the volumetric CBCT images, the three-dimensional (3D) deconvolution is performed in the image domain. Wang *et al.* [18] proposed an expectation-maximization (EM)-like iterative deblurring method to improve the spatial resolution of the spiral CT images, assuming a spatially shift-invariant linear system with a separable 3D Gaussian PSF. There are two drawbacks in the application of the iterative deblurring method. The calculation efficiency of the image domain deblurring methods is the first limiting factor for the MSI application where a large-scale volumetric data is processed. The computation load of the voxel-wise calculations in the iterative deblurring method is directly proportional to the number of the voxels, leading to long computation time in the MSI application. The second drawback is the deconvolution induced artifact, including the image noise amplification and the edge-ringing artifacts on the surrounding structures. A histogram-based selective deblurring method was proposed to suppress the deconvolution induced artifacts [20], [22], [23] in the deconvolved CT angiography (CTA) images. In addition to the 3D deconvolution operations, the histogram-based segmentations of the small high-density structures were performed in both original and deconvolved images. The deblurred image was the combination of the low-density regions segmented from the original CT image, the small high-density structures segmented from the deblurred CT image by the deconvolution operations and the transition regions replaced by the interpolation of the surrounding soft tissues. The deconvolution induced artifacts were partially suppressed after the segmentation and interpolation operations in the selective deblurring method. The complete removal of the deconvolution induced artifact was difficult in the selective deblurring method due to the inevitable inclusion of the deconvolution operations.

The applications of the existing projection domain and image domain methods for the CBCT imaging system are

limited by the complexity in the modeling of the whole system and the huge computation cost in the 3D deconvolution processes, respectively. In this work, a line integral model based deblurring method is proposed for the application of the CBCT instrument in MSI. The proposed method in the line integral domain inherits the simplicity in the modeling of the blurring effects from the image domain deblurring methods due to the linear relationship between the two domains. The deblurring model includes the deconvolution of the systematic PSF in the line integral domain. The PSF of the CBCT system is estimated by a single-parameter Gaussian function under the assumption of the rotational symmetry. The whole deblurring algorithm is applied on the 2D line integral images where the simple 2D deconvolution is performed instead of the time-consuming 3D deconvolution, leading to the higher computation efficiency and easier implementation in practice. Moreover, our deblurring operation on the line integral images can be incorporated into the streamline of the image acquisition of the CBCT equipment. The deblurred line integrals are exported for further image reconstruction. The proposed workflow is evaluated using the digital phantom, the physical phantom and the laboratory mouse in the preclinical research. To evaluate the performances of the proposed method, we compare the proposed algorithm with the existing image domain deblurring method. An image set acquired using the smaller detector pixel is generated as the reference in the comparison. The computation time is also compared between the two methods.

II. METHOD

A. DEBLURRING MODEL FOR LINE INTEGRAL IMAGES

In this work, the deblurring process is performed on each line integral prior to the CT reconstruction. Here, the line integral is the logarithmic transformation result of the projection image. The value of each pixel in the line integral image stands for the integration of the line attenuation coefficients along each line of sight. The physical processes induced blurring effects in each line integral image are depicted by the PSF of the CBCT imaging system. The blurring factors like the finite focal spot size of the x-ray tube and the pixel size of the detector are included in the PSF. The blurred line integral image is the convolutional result between the PSF and the real line integral image. The deblurring problem in the line integral domain is solved using the optimization approach with the objective function as shown below,

$$\underset{I_2}{arg\,min} \left(\left\| PSF_2 \otimes I_2 - I_2^{'} \right\|_2^2 + \gamma R_2\left(I_2\right) \right), \quad \text{subject to } I_2 \geq 0. \tag{1}$$

Here, PSF_2 stands for the 2D PSF of the CBCT system, $\otimes$ is the convolutional operator, I_2 is the 2D line integral image to be solved, $I_2^{'}$ denotes the measured image of the blurred line integral image, $R_2\left(I_2\right)$ is the regularization term, γ is the weighting factor controlling the regularization strength. The line integral image I_2 is subjected to a non-negative constraint. The objective function consists of the L_2-norm data fidelity term which penalizes the deviations of the estimated line integral image from the measured one and the regularization term which controls the compromise between the SNR and the spatial resolution. The system blur is assumed to be shift-invariant due to the rotational symmetry property around the rotation axis of the CBCT instrument. Under the shift-invariant assumption, the deblurring problem is solved using the deconvolution on each 2D line integral with the same PSF_2 as the convolutional kernel. The total variation, with the advantage of edge preserving, is applied in the regularization term.

To solve the optimization problem using the matrix operations, the objective function in (1) is rewritten as,

$$\hat{L} = \underset{L}{arg\,min} \left\| B_2 \cdot L - L^{'} \right\|_2^2 + \gamma \left\| D_2 \cdot L \right\|_1, \quad \text{subject to } L \geq 0. \tag{2}$$

Here, L, $L^{'}$, and $\hat{L}$ are the vectorized versions of the optimization variable, the measured line integrals, and the estimated line integrals, respectively. B_2 is a Toeplitz matrix converted from PSF_2. $B_2 \cdot L$ represents the same linear transformation as the 2D convolutional term $PSF_2 \otimes I_2$ in (1) [24]. D_2 is a matrix representing the 2D discrete gradient operator, $\tilde{D}_2 : R^{M\times N} \rightarrow R^{M\times N\times 2}$. The 2D discrete gradient operation under the symmetric boundary condition is defined as [25]

$$\left(\tilde{D}_2 L\right)_{i,j} = \left(L_{i+1,j} - L_{i,j}, L_{i,j+1} - L_{i,j}\right). \tag{3}$$

The regularization term is expressed as

$$R_2\left(L\right) = \sum\nolimits_{i,j} \left|L_i - L_j\right| = \left\| D_2 \cdot L \right\|_1, \tag{4}$$

where L_i, L_j are the i-th and j-th elements of the vector L.

Combining the above equations, we formulate the deblurring problem as the minimization of a convex objective function. In this work, the overrelaxed Chambolle-Pock algorithm [26], [27] is employed to solve the deblurring problem due to its superiorities in convergence speed and computational efficiency.

III. SOLVER FOR THE DEBLURRING PROBLEM

The overrelaxed Chambolle-Pock algorithm [26] solves the convex optimization problems with a canonical form,

$$\underset{x}{arg\,min}\ F\left(Kx\right) + G(x), \tag{5}$$

where F and G are convex, lower semi-continuous functions, K is a continuous linear operator. The optimization problem described by (5) is solved using the following iterations,

$$\begin{cases} \bar{x}^k = prox_{tG}\left(x^{k-1} - tK^T z^{k-1}\right) \\ \bar{z}^k = prox_{sF^*}\left(z^{k-1} + sK\left(2x^k - 2x^{k-1}\right)\right) \\ x^k = x^{k-1} + \rho\left(\bar{x}^k - x^{k-1}\right) \\ z^k = z^{k-1} + \rho\left(\bar{z}^k - z^{k-1}\right), \end{cases} \tag{6}$$

where ρ is the relaxation parameter, t and s represent the two step sizes, x and z represent the primal-dual pair. The value

of the relaxation parameter is between 0 and 2 to achieve the balance between the overrelaxed and underrelaxed operations. The proximal mapping of the function $G(u)$ with the parameter t (i.e., $prox_{tG}(x)$) is defined as

$$prox_{tG}(x) = \underset{u}{arg\,min}\left(G(u) + \frac{1}{2t}\|u - x\|_2^2\right), \tag{7}$$

The function F^* denotes the "convex conjugate" of the function F. F^* is defined as

$$F^*(z) = \sup_x\left(z^T x - F(x)\right), \tag{8}$$

The functions F and G are assumed to be the simple functions which are the real-valued functions over the subsets of the lines whose points are the real numbers. Since the proximity operators of the simple function either have a closed-form or at least can be solved efficiently with high precision, an explicit iterative relation is obtained using the overrelaxed Chambolle-Pock algorithm under the simple function assumptions of F and G. Using the constraint of $ts\|K\|^2 \le 1$, the convergence of the objective function towards the global minimum is proved in [26]. We choose $ts\|K\|^2 = 1$ in this work to maximize the initial step size and simplify each iteration by setting t or s in (6).

To apply the overrelaxed Chambolle-Pock algorithm in the 2D line integral domain, the matrix K and the functions F, G are rewritten using the elements introduced in the objective function (2) as

$$K = \begin{bmatrix} B_2 \\ D_2 \end{bmatrix}, \tag{9}$$

$$G(L) = \begin{cases} 0 & if\ L \ge 0 \\ \infty & otherwise, \end{cases} \tag{10}$$

$$F(KL) = F\left(\begin{bmatrix} B_2 L \\ D_2 L \end{bmatrix}\right) = F_1(B_2 L) + F_2(D_2 L), \tag{11}$$

$$F_1(y_1) = \left\|y_1 L'\right\|_2^2/2, \tag{12}$$

$$F_2(y_2) = \gamma\|y_2\|_1. \tag{13}$$

According to the above definitions, the proximal mappings of the functions F^* and G are

$$prox_{tG}(L) = P_+(L), \tag{14}$$

$$prox_{sF_1^*}(z_1) = \left(z_1 - sL'\right)/(1+s), \tag{15}$$

$$prox_{sF_2^*}(z_2) = P_{\gamma B}(z_2), \tag{16}$$

where P_+ represents the point-wise projections onto the non-negative orthant, $P_{\gamma B}$ denotes the point-wise projections onto the ball $\gamma B = \{\|x\|_\infty \le \gamma\}$. A separable sum rule [28] allows for

$$prox_{sF^*}\left(\begin{bmatrix} z_1 \\ z_2 \end{bmatrix}\right) = \begin{bmatrix} prox_{sF_1^*}(z_1) \\ prox_{sF_2^*}(z_2) \end{bmatrix}. \tag{17}$$

The iterative forms of the overrelaxed Chambolle-Pock algorithm in the 2D line integral domain are retrieved by combining (6) and from (14) to (17):

$$\begin{cases} \bar{L}^k = P_+\left(L^{k-1} - t\left(B_2^T z_1^{k-1} + D_2^T z_2^{k-1}\right)\right) \\ \bar{z}_1^k = \left(z_1^{k-1} + sB_2\left(2L^k - 2L^{k-1}\right) - sL'\right)\Big/(1+s) \\ \bar{z}_2^k = P_{\gamma B}\left(z_2^{k-1} + sD_2\left(2L^k - 2L^{k-1}\right)\right) \\ L^k = \rho\bar{L}^k + (1-\rho)L^{k-1} \\ z_1^k = \rho\bar{z}_1^k + (1-\rho)z_1^{k-1} \\ z_2^k = \rho\bar{z}_2^k + (1-\rho)z_2^{k-1}, \end{cases} \tag{18}$$

The length of the vectorized line integral L equals the total number of pixels in the line integral image. The second dimension of the converted Toeplitz matrix B_2 is the same as the length of L, leading to complexity in writing the explicit form of B_2. To simplify the calculation, the convolution is expressed by the point-wise product in the frequency domain instead of the matrix multiplication in the real domain. According to the convolution theorem [29], the convolution calculated by the matrix multiplication is expressed by the inverse Fourier transform (IFT) of the point-wise products of the FTs of the two convolution kernel functions:

$$B_2 \cdot L = IFT\left(FT\left(PSF_2\right).*FT\left(I_2\right)\right), \tag{19}$$

where L is the vectorized 2D line integration image I_2, "$.*$" denotes the pixel-wise multiplication. Analogously, the multiplication of B_2^T and z (vectorized I_z) is expressed using the FT operations on PSF_2 and I_z as

$$B_2^T \cdot z = IFT\left(Conj\left(FT\left(PSF_2\right)\right).*FT\left(I_z\right)\right), \tag{20}$$

where $Conj(x)$ calculates the conjugate of every element in x. The FT of the PSF is defined as the optical transfer function (OTF). The simplified expressions of (19) and (20) can be retrieved after replacing $FT\left(PSF_2\right)$ by OTF_2.

To avoid the periodic boundary condition requirement in the application of the convolution theorem, we introduce a weighting matrix in the data fidelity term $\left\|B_2 \cdot L - L'\right\|_2^2$ in (2) as

$$\left\|M(B_2 \cdot L - L')\right\|_2^2, \tag{21}$$

where M represents the diagonal matrix applying no penalties on the boundary pixels in the line integral image. The unity weights are assigned to the inner pixels of the image. The PSF and the line integral image are zero padded by the weighting matrix accordingly. The objective function (2) is thus reformulated as,

$$\hat{L} = \underset{L}{arg\,min}\left\|M(B_2 \cdot L - L')\right\|_2^2 + \gamma\|D_2 \cdot L\|_1, \quad \text{subject to } L \ge 0. \tag{22}$$

By denoting $\bar{B}_2 = MB_2$ and $\bar{L}' = ML'$, (22) is mathematically equivalent to (2). Analogously, the optimization problem with the objective function (22) can be solved using the same form of the iterations as (6) when B_2 and L' are substituted by $\bar{B}_2$ and $\bar{L}'$. Taking the boundary conditions into

consideration, we solve the deblurring problem in the 2D line integral domain using the following iterative scheme:

$$\begin{cases} \bar{L}^k = P_+\left(L^{k-1} - t\left(B_2^T M^T z_1^{k-1} + D_2^T z_2^{k-1}\right)\right) \\ \bar{z}_1^k = \left(z_1^{k-1} + sMB_2\left(2L^k - 2L^{k-1}\right) - sML'\right) \Big/ (1+s) \\ \bar{z}_2^k = P_{\gamma B}\left(z_2^{k-1} + sD_2\left(2L^k - 2L^{k-1}\right)\right) \\ L^k = \rho \bar{L}^k + (1-\rho) L^{k-1} \\ z_1^k = \rho \bar{z}_1^k + (1-\rho) z_1^{k-1} \\ z_2^k = \rho \bar{z}_2^k + (1-\rho) z_2^{k-1}. \end{cases} \tag{23}$$

A. WORKFLOW OF THE PROPOSED METHOD

The schematic of the workflow of the proposed deblurring method in the line integral domain is shown in Fig. 1. The proposed method starts with the calculation of the line integral images from the projections by the logarithmic transformation. The blurring effects in each line integral image are described by the Gaussian-type PSF of the CBCT system. The proposed deblurring method is applied to each line integral image. The deblurring problem of the line integral image is solved by the overrelaxed Chambolle-Pock algorithm as described above. Finally, the deblurred CT images are reconstructed from the deblurred line integral images.

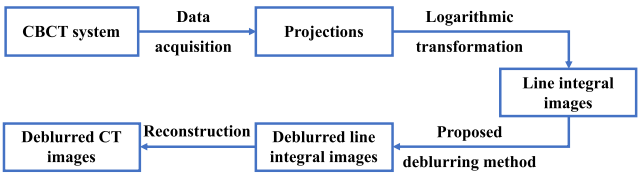

FIGURE 1. The schematic of the workflow of the proposed method.

IV. EVALUATION

A. DATA ACQUISITION

The proposed method in the line integral domain is evaluated using digital phantom, mouse phantom data, and laboratory mouse data. Two image sets of different spatial resolutions are retrieved in each case. The low-resolution image set is deblurred by the proposed method. In the meanwhile, the high-resolution image set is chosen as the reference.

The digital phantom contains a number of different regions which include the following tissue type and attenuation values obtained from the National Institute of Standards and Technology (NIST) database [30]: (i) fat ($\mu = 0.01875\ mm^{-1}$); (ii) muscle ($\mu = 0.02150\ mm^{-1}$); and (iii) bone ($\mu = 0.03\ \text{mm}^{-1}$). In addition to the three types of tissues, four sets of (iv) line pairs ($\mu = 0.03\ mm^{-1}$) with spatial frequencies of 16.7, 12.5, 10.0, and 18.3 line pairs per centimeter (lp/cm) are also included in the digital phantom. The low-resolution line integral images are obtained by projecting the digital phantom with a 0.025 mm voxel size to the pseudo-detector with a 0.4 mm pixel. Meanwhile, the 0.2 mm pixel is used in the high-resolution case. The Poisson noise of a similar level as the bench experiments is added to each line integral image [31].

The cylinder-shaped mouse phantom consists of a central cylinder of Teflon to mimic the spine, two cylindrical cavities as the thorax, and the uniform cylindrical body of polystyrene to simulate the muscle and other soft tissues. The two cavities are symmetrically distributed on both sides of the central Teflon. The length and diameter of the cylindrical body of the mouse phantom are 100 mm and 30 mm, respectively. The dimension of the laboratory mouse is similar to that of the mouse phantom.

The mouse phantom and the laboratory mouse are scanned on the test-bench CBCT instrument in our laboratory. The bench CBCT consists of the RAD-94 x-ray tube (Varian), the XRD-1611 flat panel detector (Perkin Elmer), and the customized motion and supporting structures. The focal spot size of the source is 0.4 mm. The source settings include 60 kVp and 30 mA for the mouse phantom and 50 kVp and 30 mA for the laboratory mouse. The low-resolution line integral images are obtained under the binning-3 setting of the detector with 512 by 512 pixels and a 0.4 mm pixel. Meanwhile, the binning-2 setting of the detector with 1024 by 1024 pixels and a 0.2 mm pixel is used in the high-resolution case. The geometry setup in the bench experiments includes 945.2 mm as the source to detector distance (SID) and 588.3 mm as the source to axis distance (SAD). The number of the projections is 502 for each CT scan in which the angle of each projection is evenly spaced at 0.7157 degree. The line integral image is generated from the logarithmic transformation of each projection. The voxel sizes of the reconstructed images are 0.1 mm in both low-resolution and high-resolution cases.

B. COMPARISON STUDY

To evaluate the performance of the proposed deblurring method in the line integral domain, we compare the proposed method with the reference deblurring method in the 3D image domain. The deblurring issues in the 3D image domain are solved by the same overrelaxed Chambolle-Pock algorithm as the one for the 2D line integral domain. The iterative scheme in (23) is extended to the 3D case as shown in the following:

$$\begin{cases} \bar{\mu}^k = P_+\left(\mu^{k-1} - t(B_3^T M^T z_1^{k-1} + D_3^T z_2^{k-1})\right) \\ \bar{z}_1^k = \left(z_1^{k-1} + sMB_3\left(2\mu^k - 2\mu^{k-1}\right) - sM\mu'\right) \Big/ (1+s) \\ \bar{z}_2^k = P_{\gamma B}\left(z_2^{k-1} + sD_3\left(2\mu^k - 2\mu^{k-1}\right)\right) \\ \mu^k = \rho \bar{\mu}^k + (1-\rho)\mu^{k-1} \\ z_1^k = \rho \bar{z}_1^k + (1-\rho) z_1^{k-1} \\ z_2^k = \rho \bar{z}_2^k + (1-\rho) z_2^{k-1}, \end{cases} \tag{24}$$

where μ^k, μ' and $\bar{\mu}^k$ are vectorized 3D image, B_3 is the 3D PSF matrix, D_3 is the matrix form of the 3D discrete gradient operator $\tilde{D}_3$ [25] defined as

$$\left(\tilde{D}_3 L\right)_{i,j} = \left(L_{i+1,j,k} - L_{i,j,k}, L_{i,j+1,k} - L_{i,j,k}, L_{i,j,k+1} - L_{i,j,k}\right). \tag{25}$$

The proposed deblurring method is applied to the line integral images prior to the CT reconstruction. The 3D image domain deblurring method is applied to the reconstructed CT images. The CT reconstruction is implemented using the standard FDK algorithm [32] in all the studies.

C. IMAGE QUALITY METRICS

To enable a quantitative comparison between the proposed method and the reference method, the performances of the two methods are evaluated using the metrics of the image quality, including the 2D noise power spectrum (NPS) in a uniform region of interest (ROI) and the MTF_{task} and the structural similarity index (SSIM) of a high-contrast ROI.

To evaluate the noise characteristics of the proposed scheme in the frequency domain, we quantify the 2D NPS in the deblurred images. The 2D NPS was calculated within a single-material area of the CT image using the formulation as in the following [33]:

$$NPS \approx |DFT_2\{f\}|^2, \tag{26}$$

where f equals the 2D array of the pixel values minus the mean value in the area, and DFT_2 denotes the 2D discrete Fourier transform.

The spatial resolutions of the CT imaging systems are evaluated using the task-based modulation transfer function (MTF) MTF_{task} proposed by Richard *et al.*[34]. To compute the MTF_{task}, a one-dimensional (1D) ESF is first generated by the averaging over the radial directions of the circular disk image. The differentiated ESF as the PSF is Fourier transformed to generate the MTF. To characterize the resolution of the imaging system in a scalar form, the spatial frequency f_{50} at which $MTF(f)$ is reduced to 50% is chosen as the metric to quantify the spatial resolution [34]. In addition to the MTF_{task}, the SSIM is computed in the same ROI to assess the deviation of the structures from the reference image. The SSIM of two images a and b is normally expressed as,

$$SSIM(a,b) = \frac{(2\mu_a\mu_b + C_1)(2\sigma_{ab} + C_2)}{(\mu_a^2 + \mu_b^2 + C_1)(\sigma_a^2 + \sigma_b^2 + C_2)}, \tag{27}$$

where $\mu_{a,b}, \sigma_{a,b}, \sigma_{ab}$ are the local means, standard deviations, and cross-covariance for the images a and b, respectively.

V. RESULTS

A. SIMULATION STUDIES

The cylindrical digital phantom consists of four types of area as shown in Fig. 2(a), including the oval-shaped muscle, the round-shaped bone, the four line pairs, and the other fat area. To intuitively assess the spatial resolution of each CT image, the zoom-in display of the line pairs in the ROI1 is attached to the bottom of each subfigure in Fig. 2. The first row in Fig. 2 includes the high-resolution CT image as the reference and the low-resolution image to be processed. The line pair with the highest spatial resolution is not distinguishable in the low-resolution image. The second row in Fig. 2 presents the two deblurred CT images using the proposed method in the line integral domain and the 3D overrelaxed Chambolle-Pock method in the image domain for comparison purpose, respectively. The visibility of the line pairs in both deblurred CT images is comparable with the high-resolution reference due to the improvement of the spatial resolution.

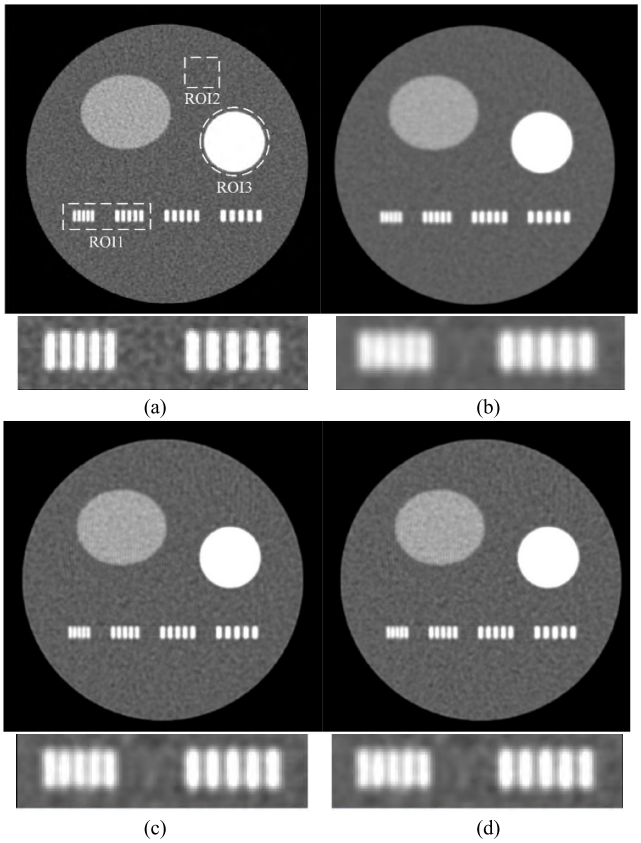

FIGURE 2. Cross-sectional CT images of the digital phantom: (a) the high-resolution image as the reference, (b) the low-resolution image to be processed, (c) the deblurred image using the proposed method, (d) the deblurred image using the 3D image domain method. The zoom-in display of the line pairs in the ROI1 of (a) is located under each subfigure. ROI2 is marked by the dashed box in the uniform area of fat. ROI3 represents the high-contrast bone region enclosed by the dashed circle. The display window is [0.015, 0.025] mm^{-1}.

The evaluation of the noise characteristics is performed in the single-tissue ROI2 in Fig. 2(a). As shown in Fig. 3, the noise distribution of the high-resolution image covers more high spatial frequency region compared to the low-resolution case, indicating more balanced frequency resolving abilities due to the higher spatial resolution. The extension of the NPS in the deblurred images compared to the low-resolution case represents the ability to recover the finer structures. The NPS of the ROIs in the two deblurred images are close to each other, suggesting the equivalent noise characteristics of the two methods. Since there are no variations in the mean values of the ROIs in the deblurred CT images compared to the high-resolution and low-resolution images, the CT number error due to the deblurring processes is negligible. The MTFs in the image

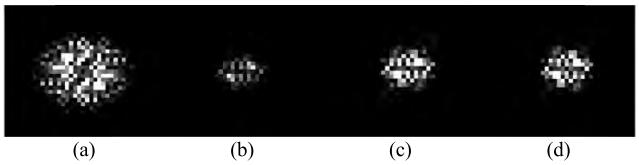

FIGURE 3. Measured NPS of the CT images of the digital phantom in Fig. 2: (a) the high-resolution image as the reference, (b) the low-resolution image to be processed, (c) the deblurred slice using the proposed method, (d) the deblurred image using the 3D image domain method. Zero frequency is at the center of each NPS.

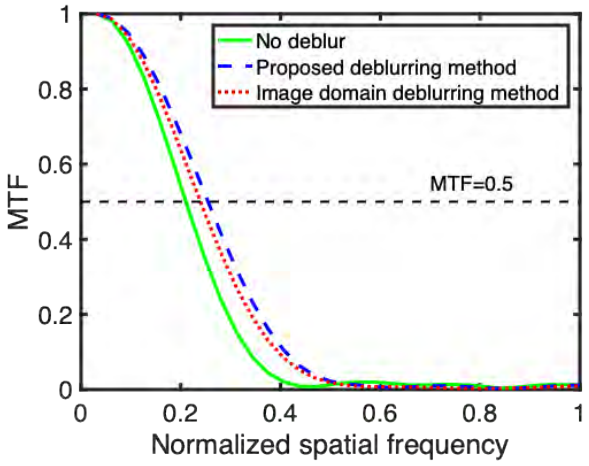

FIGURE 4. MTFs of the CT images of the digital phantom in Fig. 2: green line: low-resolution image to be processed; blue dashed line: proposed method; red dotted line: image domain method. The black dashed line represents MTF=0.5.

slices are calculated in the selected disk marked by the dashed circle and named as ROI3 in Fig.2 (a). The MTFs of the low-resolution CT image without deblurring and the two deblurred images are shown in Fig. 4. The f_{50} of the deblurred image by the 3D image domain method is 13.8% higher compared to the low-resolution image. The f_{50} of the deblurred image by the proposed method in the 2D line integral domain is 21.1% higher compared to the low-resolution case. The proposed method brings more MTF improvement compared to the image domain method. In addition to the MTF improvement, the SSIM of the proposed method is 0.9998 compared to 0.9997 in the case of the original image, indicating the slightly smaller deviation in the image structure from the reference case. The computation times of the two methods are compared in Fig. 5. The typical time cost of the proposed method is 4.6% of the image domain method.

In the digital phantom case, both deblurring methods achieve significant improvements in the spatial resolutions without degradation in the noise control performance in the deblurred images. Compared with the 3D image domain method, the proposed 2D deblurring method in the line integral domain has better deblurring performance and higher computational efficiency.

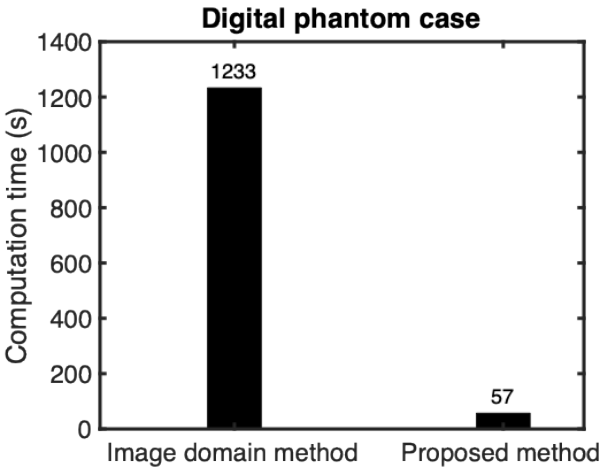

FIGURE 5. Comparison of the computation times between the proposed method and the image domain method for the digital phantom case.

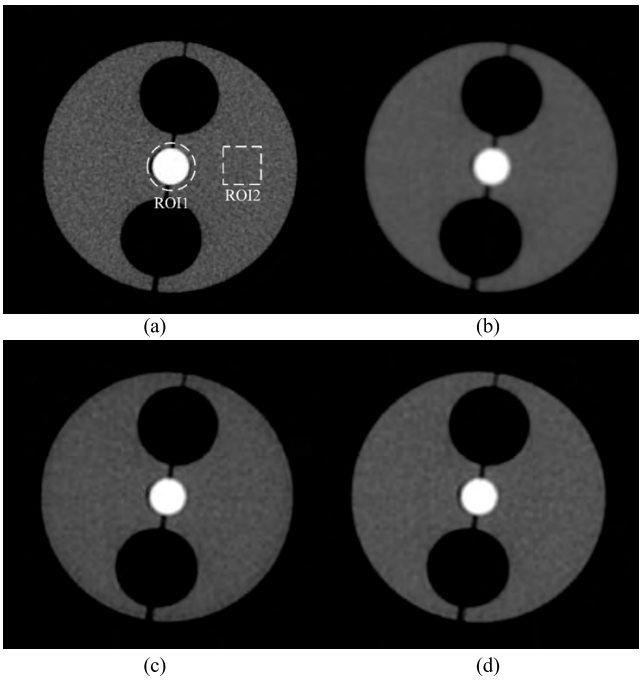

FIGURE 6. Cross-sectional CT images of the mouse phantom: (a) the high-resolution image as the reference, (b) the low-resolution image to be processed, (c) the deblurred image using the proposed method, (d) the deblurred image using the 3D image domain method. ROI1 represents the high-contrast bone region enclosed by the dashed circle. ROI2 is marked by the dashed box in the uniform area of the phantom body. The display window is [0.015, 0.055] mm^{-1}.

B. BENCH DATA OF MOUSE PHANTOM

Compared with the simulation studies, the physical objects are irradiated by the real x-rays in the bench experiments. There are more potential artifacts due to the non-ideal physical processes during the experiments. The axial and sagittal views of the mouse phantom are shown in Fig. 6 and Fig. 7, respectively. The edge sharpness of the central high-contrast

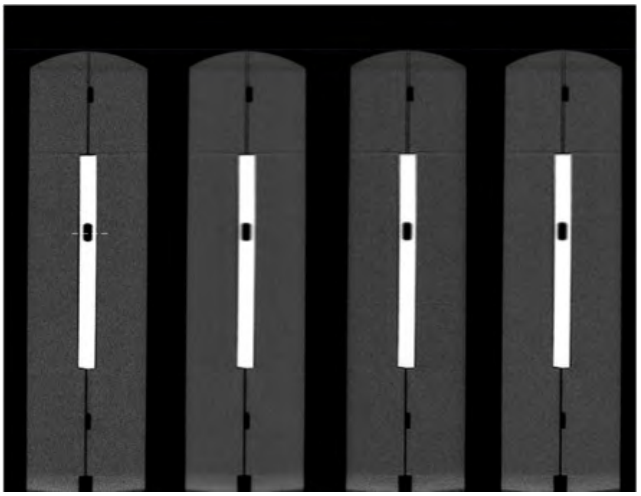

FIGURE 7. Sagittal plane CT images of the mouse phantom: (a) the high-resolution image as the reference, (b) the low-resolution image to be processed, (c) the deblurred image using the proposed method, (d) the deblurred image using the 3D image domain method. There is a dashed line in (a) indicating the location of the 1D plot in Fig. 8. The display window is [0.015, 0.055] mm^{-1}.

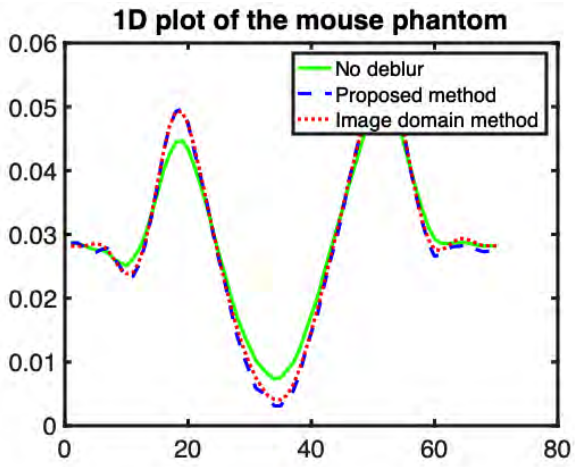

FIGURE 8. 1D horizontal profiles along the dashed line drawn in figure 6(a), green line: low-resolution image to be processed; blue dashed line: proposed method; red dotted line: image domain method.

structure (ROI1 in Fig. 6(a)) in the CBCT images is degraded by the blurring effects as shown in Fig. 6(b). The better-resolved boundaries in the second row of Fig. 6 indicate the improvements of the edge sharpness of ROI1 using the two deblurring methods. Similar improvements in the edge sharpness of the certain structures are presented in the sagittal views of the deblurred volumes as shown in Fig. 7. The 1D plots of the line segment marked by the white dashed line in Fig. 7(a) are shown in Fig. 8. The steeper peaks and valleys in the line plots of the deblurred images indicate the improvements in the spatial resolution in the sagittal plane.

The evaluation of the noise characteristics is performed in the ROI2 enclosed by a white dashed box in Fig. 6(a). As shown in Fig. 9, the noise distribution of

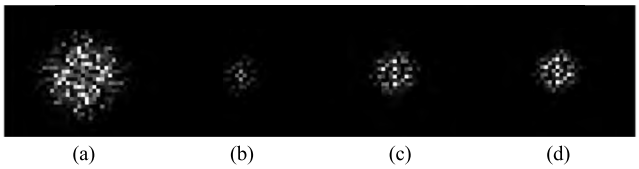

FIGURE 9. Measured NPS of the CT images of the mouse phantom in Fig. 6: (a) the high-resolution image as the reference, (b) the low-resolution image to be processed, (c) the deblurred slice using the proposed method, (d) the deblurred image using the 3D image domain method. Zero frequency is at the center of each NPS.

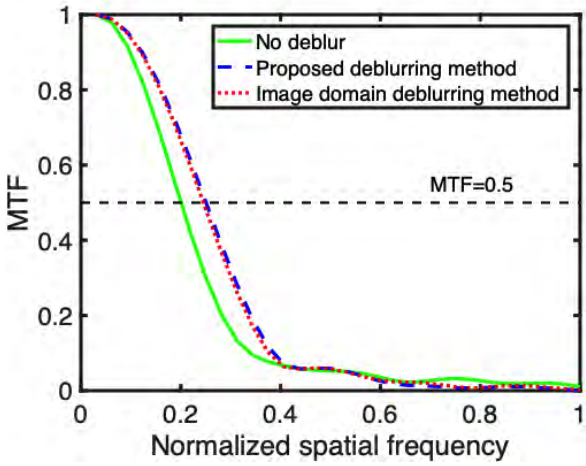

FIGURE 10. MTFs of the CT images of the mouse phantom in Fig. 6: green line: low-resolution image to be processed; blue dashed line: proposed method; red dotted line: image domain method. The black dashed line represents MTF=0.5.

the high-resolution image provides more high and medium spatial frequency components compared to the low-resolution case. The medium frequency components are recovered in the NPS of the ROIs in the two deblurred images. The NPS of the ROIs in the two deblurred images are close to each other, suggesting the equivalent noise characteristics of the two methods. According to the mean values of the ROIs in the four CT images, the CT number error due to the deblurring processes is negligible. The MTF calculation is performed in the selected disk ROI1 in Fig. 6(a). According to the MTFs shown in Fig. 10, the increases of f_{50} over the low-resolution image are 22.2% and 24.8% for the image domain and the proposed methods, respectively. In addition to the MTF improvement, the SSIMs of the proposed method and the image domain method are 0.9945 and 0.9943, respectively. The SSIM of the original image and the reference image is only 0.9913. The proposed method shows better performance in the recovery of the image structure. Fig. 11 shows the computation times of the two deblurring methods. The computation time of the proposed method is 4.4% of the image domain method.

C. BENCH DATA OF LABORATORY MOUSE

The body structure of the laboratory mouse is more complicated compared to the mouse phantom, leading to a higher requirement of the spatial resolution to resolve

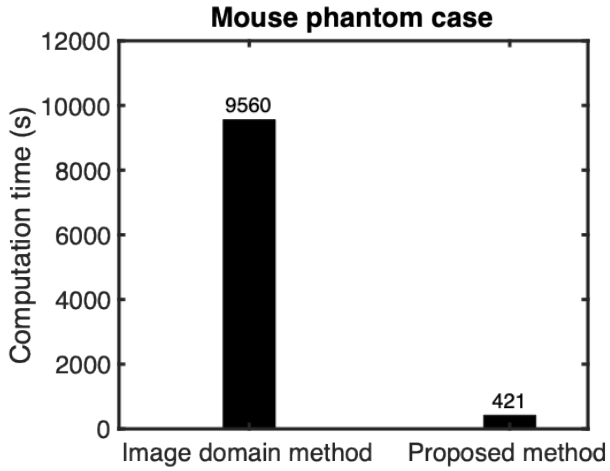

FIGURE 11. Comparison of the computation times between the proposed method and the image domain method for the mouse phantom case.

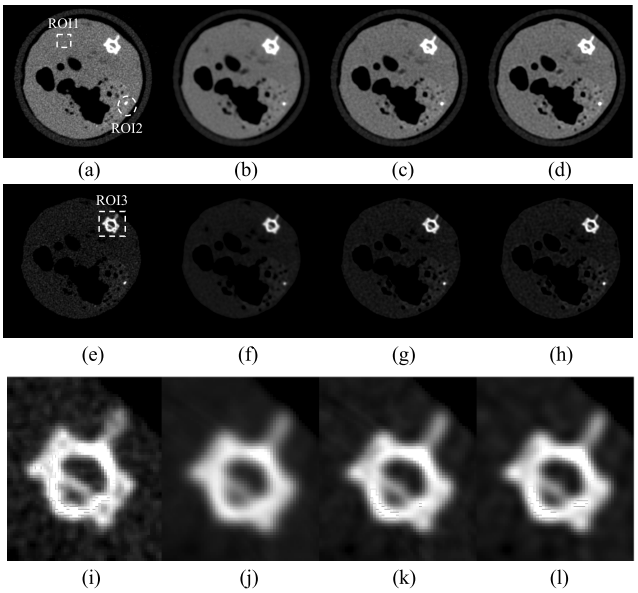

FIGURE 12. Cross-sectional CT images of the laboratory mouse: (a, e, i) the high-resolution images as the reference, (b, f, j) the low-resolution images to be processed, (c, g, k) the deblurred images using the proposed method, (d, h, l) the deblurred images using the image domain method. ROI1 represents the high-contrast bone region enclosed by the dashed circle. ROI2 is marked by the dashed box in the uniform area of the mouse body. The third row is the zoom-in display of the ROI3 enclosed by the white dashed box in (e). The display windows of the first row and the other two rows are [0.015, 0.055] mm^{-1} and [0.03, 0.07] mm^{-1}, respectively.

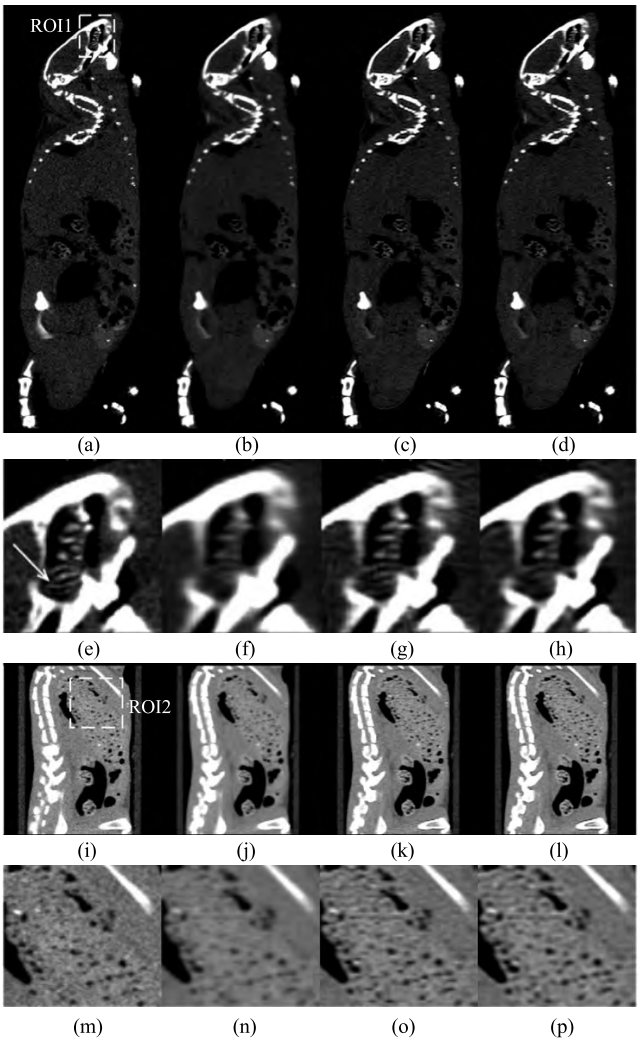

FIGURE 13. Sagittal CT images of the laboratory mouse: (a, e, i, m) the high-resolution image as the reference, (b, f, j, n) the low-resolution image to be processed, (c, g, k, o) the deblurred image using the proposed method, (d, h, l, p) the deblurred image using the image domain method. The second row is the zoom-in display of the ROI1 enclosed by the white dashed box in (a). The fourth row is the zoom-in display of the ROI2 enclosed by the white dashed box in (i). The display windows of the first and second two rows are [0.03, 0.07] mm^{-1} and [0.015, 0.055] mm^{-1}, respectively.

the micro-structures. The cross-sectional CBCT images of the laboratory mouse are presented in Fig. 12. The first two rows are the cross-sectional images where the display windows are optimized for the soft tissue and the bone, respectively. The third row is the zoom-in display of the ROI in Fig. 12 (e). The annular structure outside the soft tissue region of the laboratory mouse is the shell of the plastic container. According to the first two columns in Fig. 12, the degradation of the spatial resolution and the drop in the CT value of the bone structure are present in the low-resolution image compared to the high-resolution reference. According to the second two columns in Fig. 12, the edge sharpness of the high-contrast objects like the bones and gas pockets is improved in the deblurred images without introducing any new artifact. In addition to the cross-sectional CT images shown in Fig. 12, the sagittal and coronal views of the mouse are presented in Fig. 13 and Fig. 14, respectively.

The bone and soft tissue windows are applied to the first two and the second two rows in Fig. 13, respectively. The bone structure around the arrow mark in the zoom-in display of the mouse skull region (second row of Fig. 13) is indistinguishable before the deblurring processes. As shown in the last two columns in Fig. 13, the boundary of the bone

structure is successfully recovered after the deblurring processes. Compared to the image domain method, more details of the bone structure are recovered in the deblurred image by the proposed method, leading to a smaller gap between the deblurred image and the high-resolution reference image. There are a number of gas pockets in the rectangle ROI marked in the third row of Fig. 13 where the display window is optimized for the soft tissue. The edge sharpness of the gas pockets is improved by both deblurring methods. The improvements in the two deblurred images are comparable.

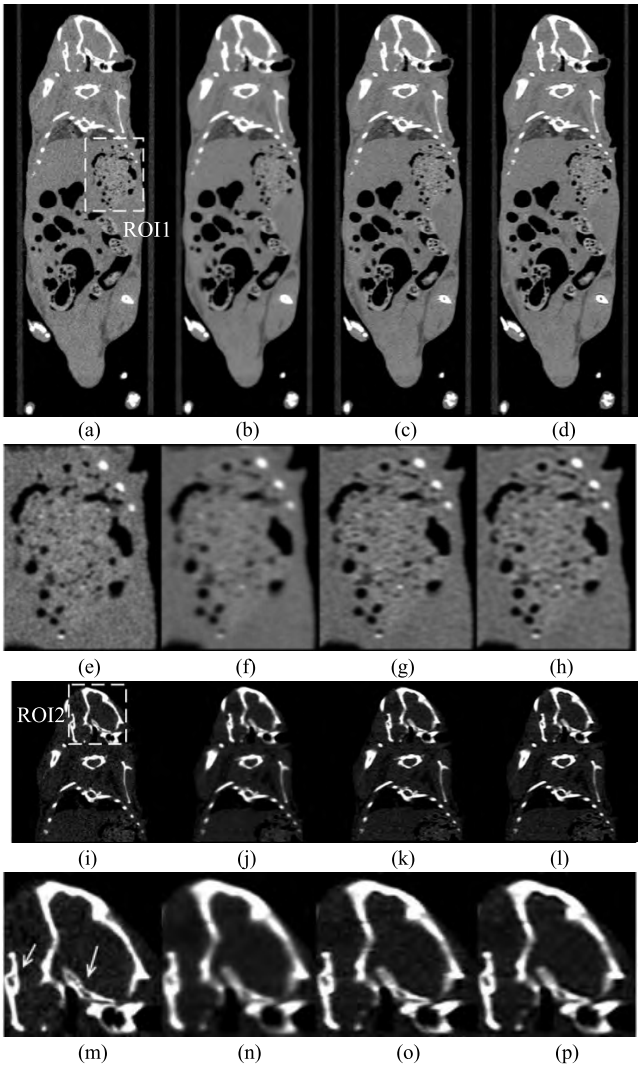

FIGURE 14. Coronal CT images of the laboratory mouse: (a, e, i, m) the high-resolution image as the reference, (b, f, j, n) the low-resolution image to be processed, (c, g, k, o) the deblurred image using the proposed method, (d, h, l, p) the deblurred image using the image domain method. The second row is the zoom-in display of the ROI1 enclosed by the white dashed box in (a). The fourth row is the zoom-in display of the ROI2 enclosed by the white dashed box in (i). The display windows of the first and second two rows are [0.015, 0.055] mm^{-1} and [0.03, 0.07] mm^{-1}, respectively.

The soft tissue and bone windows are applied to the first two and the second two rows in Fig. 14, respectively. The densely packed gas pockets in the soft tissue ROI as shown in Fig. 14(a) are blurred out in the low-resolution image. Some smaller gas pockets are very similar to the surrounding soft tissues. The recognition of the boundary of the small gas pockets is easier in the deblurred images (last two columns in Fig. 14). The edge sharpness of some gas pockets in the deblurred images is comparable with the high-resolution reference image shown in the first column of Fig. 14. The mouse skull region is selected as the ROI in the images with a display window optimized for bone. The skull structure in Fig. 14(n) is blurred, especially the bone joint. The boundaries of the joints in the deblurred images are distinguishable.

FIGURE 15. Measured NPS of the CT images of the laboratory mouse in Fig. 12: (a) the high-resolution image as the reference, (b) the low-resolution image to be processed, (c) the deblurred slice using the proposed method, (d) the deblurred image using the 3D image domain method. Zero frequency is at the center of each NPS.

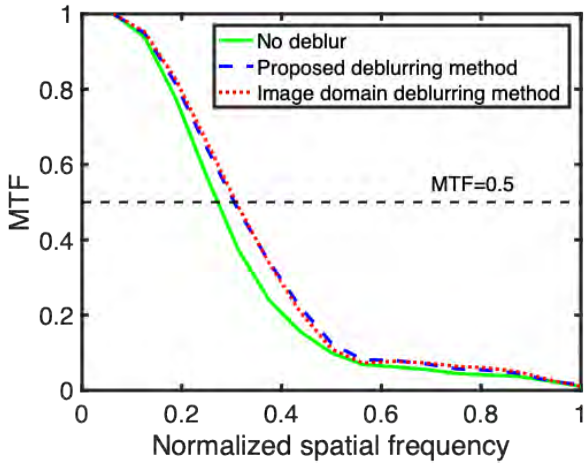

FIGURE 16. MTFs of the CT images of the laboratory mouse in Fig. 12: green line: low-resolution image to be processed; blue dashed line: proposed method; red dotted line: image domain method. The black dashed line represents MTF=0.5.

The evaluation of the noise characteristics of the proposed method is performed in the ROI2 enclosed by a white dotted box in Fig. 12(a). The missing medium frequency components in the NPS of the low-resolution image case are recovered using the two deblurring methods. Similar noise characteristics are achieved by the two deblurring methods according to the 2D NPS shown in Fig. 15. According to the mean values of the ROIs in the four CT images, the CT number errors are negligible in the deblurred CT images. The MTF calculation is performed in the ROI1 enclosed by a white dotted circle in Fig. 12(a). According to the MTFs shown in Fig. 16, the increases of f_{50} over the low-resolution image are 13.5% and 12.2% for the image domain and the proposed methods, respectively. In addition to the MTF

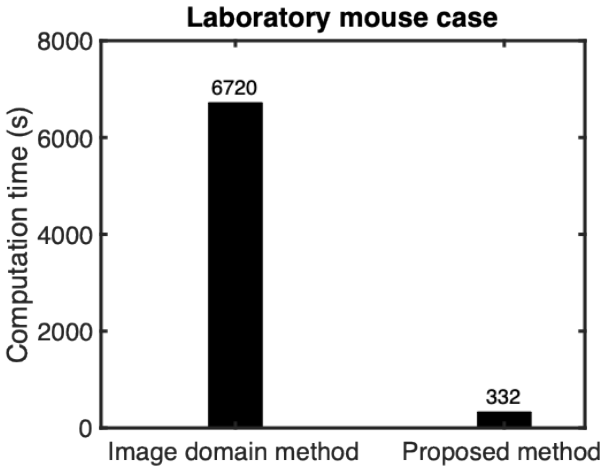

FIGURE 17. Comparison of the computation times between the proposed method and the image domain method for the laboratory mouse case.

improvement, the SSIMs of the proposed method and the image domain method are 0.9913 and 0.9911, respectively. The SSIM of the original image and the reference image is 0.9903. The proposed method shows better performance in the recovery of the image structure. The computation times of the two deblurring methods are shown in Fig. 17. The computation time of the proposed method is 4.9% of the image domain method.

VI. DISCUSSIONS

In this work, we proposed a deblurring method in the line integral domain. The deblurring problem is transformed into an iterative optimization problem in which the deblurred line integral images are estimated. The blurring effects in the line integral domain of the CBCT imaging system are characterized by the systematic PSF and introduced in the objective function. The systematic PSF is simplified as a Gaussian kernel function with the shift-invariant assumption of the CBCT system. To efficiently solve the optimization problem, the overrelaxed Chambolle-Pock algorithm is introduced to the iterative calculations in the 2D line integral domain. There are significant improvements in the spatial resolutions of the reconstructed images using the deblurred line integrals by the proposed method.

According to the comparison results with the reference method in the 3D image domain, the performances of the proposed and the reference methods are comparable with respect to the 2D NPS and MTF. The proposed 2D line integral deblur method outperforms the 3D method at the computational efficiency and the accessibility. The improvement in the computational efficiency is contributed by the architecture with only 2D operations. The deblurring processes for the different line integral images in the proposed method are independent of each other, leading to the ease of integration of the deblurring process in the data acquisition streamline and the acceleration potential using parallel GPU computing. The deblurred line integral images are sequentially exported to the next reconstruction process, enabling the instant retrieval of the deblurred CT image just after the data acquisition of the last frame.

In addition to the incorporation into the CT data acquisition streamline, there are other future directions for the line integral domain deblur. The in-depth comparison between the 2D and 3D deblurring methods is a near-term subject that helps with understanding the principles of the parameter optimization in the Chambolle-Pock algorithm. The automation of the parameter optimization in the Gaussian kernel function is also important in extending the application of the proposed method towards the CT systems with more complexity in the PSF and the blurring factors.

In current work, the shift-invariant assumption of the imaging system is the prerequisite of the modeling of the PSF by a simple Gaussian kernel function. The irregular shape of the x-ray tube focal spot and the fact that the source blur is depth-dependent result in the variations of the PSF in the system. We will include the explicit characterization of the source blur in the modeling of the PSF of the CBCT.

In our 2D deblur model, line integral images of different angles are assumed to be independent, whereas the afterglow phenomenon during the scan could lead to the correlations between the adjacent projections. We will use a 3D PSF kernel in which the third dimension represents the different projection angles to characterize the blurring effects brought by the afterglow phenomenon.

VII. CONCLUSION

In summary, the 2D deblurring method described in this work provides an efficient solution to the deblurring problems in the MSI using the CBCT system. The proposed method employs a simple objective function design in which all the blurring factors are characterized together by the PSF of the CT imaging system. According to the evaluation results in different samples, the proposed method successfully improves the spatial resolution without the degradation of the noise performance compared with the 3D image domain method. Moreover, the computation time of the proposed method is 20 times shorter than the conventional image domain deblurring method, leading to potential incorporation of the proposed deblurring workflow with the image acquisition streamline of the CT instrument. Owing to the above advantages, the proposed method is practical and attractive for the deblurring of the CBCT images in MSI.

ACKNOWLEDGMENT

Chen Luo and Qiao Liu contributed equally to this work.

DISCLOSURES

All authors declare no financial and non-financial competing interests.

REFERENCES

[1] R. Gupta *et al.*, "Flat-panel volume CT: Fundamental principles, technology, and applications," *Radiographics*, vol. 28, no. 7, pp. 2009–2022, Nov./Dec. 2008.
[2] M. J. Paulus, S. S. Gleason, S. J. Kennel, P. R. Hunsicker, and D. K. Johnson, "High resolution X-ray computed tomography: An emerging tool for small animal cancer research," *Neoplasia*, vol. 2, pp. 62–70, Jan. 2000.
[3] M. L. Bouxsein, S. K. Boyd, B. A. Christiansen, R. E. Guldberg, K. J. Jepsen, and R. Müller, "Guidelines for assessment of bone microstructure in rodents using micro-computed tomography," *J. Bone Miner Res.*, vol. 25, no. 7, pp. 1468–1486, Jul. 2010.
[4] J. H. Siewerdsen *et al.*, "A simple, direct method for X-ray scatter estimation and correction in digital radiography and cone-beam CT," *Med. Phys.*, vol. 33, no. 1, pp. 187–197, Jan. 2006.
[5] L. Zhu, Y. Xie, J. Wang, and L. Xing, "Scatter correction for cone-beam CT in radiation therapy," *Med. Phys.*, vol. 36, no. 6, pp. 2258–2268, Jun. 2009.
[6] T. Niu and L. Zhu, "Scatter correction for full-fan volumetric CT using a stationary beam blocker in a single full scan," *Med. Phys.*, vol. 38, no. 11, pp. 6027–6038, Nov. 2011.
[7] M. van Herk, L. Ploeger, and J.-J. Sonke, "A novel method for megavoltage scatter correction in cone-beam CT acquired concurrent with rotational irradiation," *Radiotherapy Oncol.*, vol. 100, no. 3, pp. 365–369, Sep. 2011.
[8] Y. Xu *et al.*, "A practical cone-beam CT scatter correction method with optimized Monte Carlo simulations for image-guided radiation therapy," *Phys. Med. Biol.*, vol. 60, no. 9, pp. 3567–3587, May 2015.
[9] J. Hsieh, R. C. Molthen, C. A. Dawson, and R. H. Johnson, "An iterative approach to the beam hardening correction in cone beam CT," *Med. Phys.*, vol. 27, no. 1, pp. 9–23, Jan. 2000.
[10] F. G. Draenert, E. Coppenrath, P. Herzog, S. Müller, and U. G. Mueller-Lisse, "Beam hardening artefacts occur in dental implant scans with the NewTom cone beam CT but not with the dental 4-row multidetector CT," *Dentomaxillofac Radiol.*, vol. 36, no. 4, pp. 198–203, May 2007.
[11] J. S. Maltz *et al.*, "Algorithm for X-ray scatter, beam-hardening, and beam profile correction in diagnostic (kilovoltage) and treatment (megavoltage) cone beam CT," *IEEE Trans. Med. Imag.*, vol. 27, no. 12, pp. 1791–1810, Dec. 2008.
[12] I. Reitz, B. M. Hesse, S. Nill, T. Tücking, and U. Oelfke, "Enhancement of image quality with a fast iterative scatter and beam hardening correction method for kV CBCT," *Zeitschrift Med. Phys.*, vol. 19, no. 3, pp. 158–172, Mar. 2009.
[13] Y. Li, J. Garrett, and G.-H. Chen, "Reduction of beam hardening artifacts in cone-beam CT imaging via SMART-RECON algorithm," *Proc. SPIE*, vol. 9783, p. 97830W, Mar. 2016. [Online]. Available: https://www.spiedigitallibrary.org/conference-proceedings-of-spie/9783/97830W/Reduction-of-beam-hardening-artifacts-in-cone-beam-CT-imaging/10.1117/12.2216882.short?SSO=1
[14] I. Mori, Y. Machida, M. Osanai, and K. Iinuma, "Photon starvation artifacts of X-ray CT: Their true cause and a solution," *Radiol. Phys. Technol.*, vol. 6, no. 1, pp. 130–141, Jan. 2013.
[15] J. T. Bushberg, *The Essential Physics of Medical Imaging*, 3rd ed. Philadelphia, PA, USA: Williams & Wilkins, 2012, p. 1030.
[16] S. Tilley II, J. H. Siewerdsen, and J. W. Stayman, "Model-based iterative reconstruction for flat-panel cone-beam CT with focal spot blur, detector blur, and correlated noise," *Phys. Med. Biol.*, vol. 61, no. 1, pp. 296–319, 2016.
[17] J. A. Meganck, K. M. Kozloff, M. M. Thornton, S. M. Broski, and S. A. Goldstein, "Beam hardening artifacts in micro-computed tomography scanning can be reduced by X-ray beam filtration and the resulting images can be used to accurately measure BMD," (in English), *Bone*, vol. 45, no. 6, pp. 1104–1116, Dec. 2009.
[18] G. Wang, M. W. Vannier, M. W. Skinner, M. G. P. Cavalcanti, and G. W. Harding, "Spiral CT image deblurring for cochlear implantation," *IEEE Trans. Med. Imag.*, vol. 17, no. 2, pp. 251–262, Apr. 1998.
[19] M. Jiang, G. Wang, M. W. Skinner, J. T. Rubinstein, and M. W. Vannier, "Blind deblurring of spiral CT images," *IEEE Trans. Med. Imag.*, vol. 22, no. 7, pp. 837–845, Jul. 2003.
[20] E. Rollano-Hijarrubia, R. Manniesing, and W. J. Niessen, "Selective deblurring for improved calcification visualization and quantification in carotid CT angiography: Validation using micro-CT," *IEEE Trans. Med. Imag.*, vol. 28, no. 3, pp. 446–453, Mar. 2009.
[21] Z. Chen and R. Ning, "Three-dimensional point spread function measurement of cone-beam computed tomography system by iterative edge-blurring algorithm," *Phys. Med. Biol.*, vol. 49, no. 10, pp. 1865–1880, May 2004.
[22] J. Nuyts, B. De Man, J. A. Fessler, W. Zbijewski, and F. J. Beekman, "Modelling the physics in the iterative reconstruction for transmission computed tomography," (in English), *Phys. Med. Biol.*, vol. 58, no. 12, pp. R63–R96, Jun. 2013.
[23] E. Rollano-Hijarrubia, W. Niessen, H. Weinans, A. van der Lugt, and R. Stokking, "Histogram-based selective deblurring to improve computed tomography imaging of calcifications," *Invest. Radiol.*, vol. 42, no. 1, pp. 8–22, Jan. 2007.
[24] P. C. Hansen, "Deconvolution and regularization with Toeplitz matrices," (in English), *Numer. Algorithms*, vol. 29, no. 4, pp. 323–378, Apr. 2002.
[25] L. Condat, "Discrete total variation: New definition and minimization," (in English), *SIAM J. Imag. Sci.*, vol. 10, no. 3, pp. 1258–1290, Mar. 2017.
[26] L. Condat, "A primal–dual splitting method for convex optimization involving Lipschitzian, proximable and linear composite terms," *J. Optim. Theory Appl.*, vol. 158, no. 2, pp. 460–479, Feb. 2013.
[27] A. Chambolle and T. Pock, "A first-order primal-dual algorithm for convex problems with applications to imaging," *J. Math. Imag. Vis.*, vol. 40, no. 1, pp. 120–145, 2011.
[28] S. Boyd and L. Vandenberghe, *Convex Optimization*. Cambridge, U.K.: Cambridge Univ. Press, 2004, p. 1859.
[29] A. V. Oppenheim and A. S. Willsky, *Signals and Systems*. London, U.K.: Pearson, 2013.
[30] J. H. Hubbell and S. M. Seltzer, "Tables of X-ray mass attenuation coefficients and mass energy-absorption coefficients 1 keV to 20 MeV for elements Z = 1 to 92 and 48 additional substances of dosimetric interest," NIST Phys. Lab., Gaithersburg, MD, USA, Tech. Rep. PB-95-220539/XAB; NISTIR-5632 TRN: 51812148, 1996. [Online]. Available: https://www.osti.gov/biblio/76335
[31] H. Gao, "Fast parallel algorithms for the X-ray transform and its adjoint," *Med. Phys.*, vol. 39, no. 11, pp. 7110–7120, Nov. 2012.
[32] L. A. Feldkamp, L. C. Davis, and J. W. Kress, "Practical cone-beam algorithm," *J. Opt. Soc. Amer. A, Opt. Image Sci.*, vol. 1, no. 6, pp. 612–619, 1984.
[33] M. Petrongolo and L. Zhu, "Noise suppression for dual-energy CT through entropy minimization," *IEEE Trans. Med. Imag.*, vol. 34, no. 11, pp. 2286–2297, Nov. 2015.
[34] S. Richard, D. B. Husarik, G. Yadava, S. N. Murphy, and E. Samei, "Towards task-based assessment of CT performance: System and object MTF across different reconstruction algorithms," *Med. Phys.*, vol. 39, no. 7, pp. 4115–4122, Jul. 2012.

CHEN LUO was born in Anhui, China, in 1987. He received the bachelor's degree in applied physics and Ph.D. degree in plasma physics from the University of Science and Technology of China, Hefei, China, in 2006 and 2014, respectively. He is currently a Post-Doctoral Researcher at Zhejiang University, Hangzhou, China.

From 2014 to 2015, he worked for a medical device company in China as an R&D Engineer. From 2015 to 2017, he was a Post-Doctoral Fellow at the University of California, Davis, CA, USA. His research interests include CT image processing algorithms, IGRT, cone-beam CT instrument, microwave imaging instrument, fusion plasma diagnostic, and electron cyclotron emission imaging.

QIAO LIU received the bachelor's degree in mechanical engineering from the Lanzhou University of Technology, Lanzhou, China, in 2017. He is currently pursuing the master's degree in biological physics with Zhejiang University, Hangzhou, China.

He is an expert in mechanical design of the cone-beam CT instrument. His research interests include cone-beam CT instrument, stereo vision, small animal imaging, and respiratory gating. He holds one patent.

SHUTAO GONG received the bachelor's degree in biomedical engineering from Central South University, Changsha, China, in 2015,and the master's degree in biomedical engineering from Zhejiang University, Hangzhou, China, in 2018.

His research interests include cone-beam CT instrument, small animal imaging, and low-dose reconstruction. He holds two patents.

CHUNLIN YANG received the bachelor's degree from the Lanzhou University of Technology, Lanzhou, China, in 2016. He is currently pursuing the master's degree in biological physics with Zhejiang University, Hangzhou, China.

His research interests include cone-beam CT instrument, scatter correction, Monte Carlo simulation, IGRT, 4D CBCT, deep learning in medical imaging, and low-dose reconstruction.

XIUHUA HU received the Ph.D. degree from Zhejiang University, Hangzhou, China, in 2012. She is currently an Associate Chief Physician at the Department of Radiology, Sir Run Run Shaw Hospital, Zhejiang University School of Medicine, Hangzhou.

Her research interests include the cardiothoracic imaging diagnosis and the clinical applications of the low-dose CT and CT angiography.

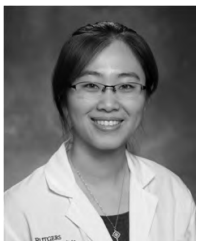

KE NIE received the B.S. degree from the University of Science and Technology of China, Hefei, China, and the Ph.D. degree from the University of California, Irvine. She is currently an Associate Professor at Rutgers University, NY, USA.

Her research interests include general radiological physics, IGRT, image registration, perfusion CT, and radiomics.

Dr. Nie is the Director of the Medical Physics Residency Program and the Director of GammaKnife Physics at the Robert Wood Johnson Medical School, Rutgers University.

TIANYE NIU received the Ph.D. degree from the University of Science and Technology of China, Hefei, China, in 2009. He is currently a Full Professor with the Zhejiang University Institute of Translational Medicine and the Affiliated Sir Run Run Shaw Hospital, Zhejiang University School of Medicine.

From 2009 to 2013, he held a post-doctoral position in the Medical Physics Program with the Georgia Institute of Technology, GA, USA. His research interests include compressed sensing, low-dose reconstruction, dual-energy CT imaging, spectral CT imaging, IGRT, proton therapy, radiomics, and cone-beam CT instrument.